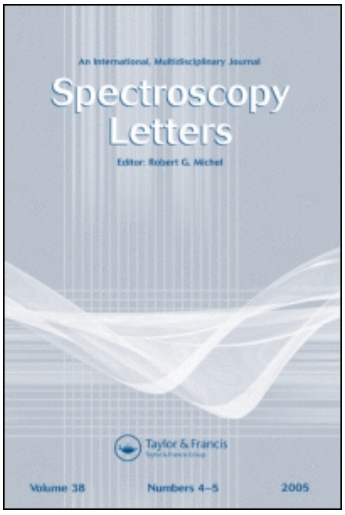

Spectroscopy Letters
Publication details, including instructions for authors and subscription information:
http://www.informaworld.com/smpp/title~content=t713597299

Analyses of $4f^{11}$ Energy Levels and Transition Intensities Between Stark Levels of Er^{3+} in $Y_3Al_5O_{12}$

Gary W. Burdick[a]; John B. Gruber[b]; Kelly L. Nash[b]; Sreerenjini Chandra[b]; Dhiraj K. Sardar[b]
[a] Department of Physics, Andrews University, Berrien Springs, MI [b] Department of Physics and Astronomy, The University of Texas at San Antonio, San Antonio, TX

Online publication date: 30 July 2010

To cite this Article Burdick, Gary W. , Gruber, John B. , Nash, Kelly L. , Chandra, Sreerenjini and Sardar, Dhiraj K.(2010) 'Analyses of $4f^{11}$ Energy Levels and Transition Intensities Between Stark Levels of Er^{3+} in $Y_3Al_5O_{12}$', Spectroscopy Letters, 43: 5, 406 — 422
To link to this Article: DOI: 10.1080/00387010.2010.487019
URL: http://dx.doi.org/10.1080/00387010.2010.487019

Spectroscopy Letters, 43:406–422, 2010

ISSN: 0038-7010 print/1532-2289 online
DOI: 10.1080/00387010.2010.487019

Taylor & Francis
Taylor & Francis Group

Analyses of $4f^{11}$ Energy Levels and Transition Intensities Between Stark Levels of Er^{3+} in $Y_3Al_5O_{12}$

Gary W. Burdick[1], John B. Gruber[2], Kelly L. Nash[2], Sreerenjini Chandra[2], and Dhiraj K. Sardar[2]

[1]Department of Physics, Andrews University, Berrien Springs, MI
[2]Department of Physics and Astronomy, The University of Texas at San Antonio, San Antonio, TX

ABSTRACT Absorption and fluorescence spectra obtained at temperatures as low as 4 K were investigated between 200 and 1550 nm on samples containing approximately 1.2 at. wt. % Er in $Y_3Al_5O_{12}$ (YAG). Within this wavelength range 125 experimental energy (Stark) levels were analyzed, representing data that span 29 $^{2S+1}L_J$ multiplet manifolds of $Er^{3+}(4f^{11})$ in D_2 sites up to an energy of 44,000 cm^{-1}. Agreement between calculated and observed Stark levels was achieved with an r.m.s. deviation of 11.2 cm^{-1}. These transitions originate from the ground-state Stark level in the $^4I_{15/2}$ manifold to $J+1/2$ Stark levels associated with each of the 28 excited-state manifolds. A total of 88 ground-state absorption transition line strengths were measured for 19 $^{2S+1}L_J$ multiplet manifolds between 280 and 1550 nm. For line strength measurements, the Er^{3+} ion is assumed to be distributed homogeneously throughout the D_2 cation sites of Y^{3+} in the lattice. The line strengths were analyzed with a weighted $(E_i - C_i)/E_i$, with an r.m.s. error of 0.25. Use of a "vector crystal field" parametrization resolves ambiguities in the transition intensity parameters and allows for the definition of polarization-resolved Judd-Ofelt parameters, which may have wide-ranging applicability for future Judd-Ofelt-type intensity calculations.

KEYWORDS

INTRODUCTION

Trivalent erbium $Er^{3+}(4f^{11})$, as a dopant in the laser host material yttrium aluminum garnet $Y_3Al_5O_{12}$ (YAG), is a well-known and popular activator ion in a medium having optical, thermal, and mechanical properties suitable for numerous photonic applications.[1–4] Stimulated emission is obtained in the near infrared and visible regions of the spectrum.[5] The output wavelengths are useful for remote sensing.[5–7] The absorption cross sections for the first excited multiplet manifold $^{2S+1}L_J$ of $Er^{3+}(4f^{11})$, namely $^4I_{13/2}$ (1440 to 1530 nm), represent some of the strongest ground-state absorption transitions observed in the spectrum, with the exception of the $^2H(2)_{11/2}$ manifold (510 to 525 nm).[8] This observation, together with a relatively long lifetime of about 6.5 ms measured from this manifold to the ground-state

Received 23 May 2009; accepted 10 July 2009.

Address correspondence to Gary W. Burdick, Department of Physics, Andrews University, Berrien Springs, MI 49104, USA.

manifold ($^4I_{15/2}$) in a 1 at. wt. % sample, along with recent technology for resonant pumping, leads to efficient eye-safe stimulated emission with high brightness, and high-power output that is welcomed in a number of current applications.[9–11]

At higher concentrations, cross-relaxation processes between erbium ions becomes important. These processes are effective in upconversion in addition to excited state absorption and photon avalanche processes.[5] Excitation brought about by these methods can lead to stimulated emission from and between other members of the ^4I_J multiplet that increase the availability of additional wavelength sources that emit further in the infrared that are being tapped currently for source and detection routines. Recent advances in the preparation and fabrication of erbium-doped YAG through methods inspired by nanotechnology provide even more opportunity to develop less expensive optical components in an economically driven business environment.

To explore the growing number of possibilities for this material as an optical device, it is appropriate to investigate the full wavelength range of spectroscopic properties of Er^{3+} in its aluminum garnet host. There are numerous studies and reviews available that contribute to the understanding of the energy-level structure of Er^{3+} in YAG over the past several decades. Early studies include the work of Koningstein et al.,[12] Zverev et al.,[13] and Kaminskii et al.[14] Reviews have been written by Kaminskii,[1] Morrison and Leavitt,[15] and others. A detailed analysis of the crystal-field energy-level structure of $Er^{3+}(4f^{11})$ in different garnet hosts was carried out by Gruber et al.[16] and an analysis of manifold-to-manifold absorption intensities and emission cross sections for selected laser transitions were reported recently by Sardar et al.[8] for Er^{3+} in the nanocrystalline ceramic YAG.

In the present study, we provide a comprehensive review of all the energy (Stark) levels of $Er^{3+}(4f^{11})$ in YAG and the intensity of the ground state absorption from the ground-state Stark level to individual excited Stark levels having an energy up to 50,000 cm^{-1}. Within this energy range, 125 experimental Stark levels covering a span of 29 $^{2S+1}L_J$ multiplet manifolds are analyzed in detail up to 44,000 cm^{-1} with an r.m.s. deviation of 11.2 cm^{-1}. Several experimental Stark levels not identified earlier have been analyzed and included within the reported listing. The 88 ground state absorption line strengths measured for 19 $^{2S+1}L_J$ multiplet manifolds between 6500 and 35,000 cm^{-1} are analyzed with a weighted, $(E_i - C_i)/E_i$, r.m.s. error of 0.25. Details of both the energy level and transition line strength calculations are given. Use of the "vector crystal field" parametrization for transition line strengths resolves ambiguities in the transition intensity parameters. The vector crystal field parametrization also leads to a definition for polarization-resolved Judd-Ofelt parameters, which may have wide-ranging applicability for future Judd-Ofelt-type intensity calculations.

EXPERIMENTAL DETAILS

Single crystals of yttrium aluminum garnet ($Y_3Al_5O_{12}$, YAG) used in the present study were grown by Milan Kokta using a modified Czochralski method.[17,18] The aluminum garnet melts congruently at 1970°C, a temperature several hundred degrees lower than required to grow either the sesquioxide or the orthoaluminate form of either yttrium or erbium. The crystals were grown in a dry, argon atmosphere and contained approximately 1.2 at. wt. % erbium. The erbium concentration was established based on a distribution coefficient of 0.96 and the dopant concentration in the melt. To confirm the erbium concentration in the crystals, the spectroscopic samples were analyzed chemically using ion exchange and plasma excitation methods. These independent results gave an erbium concentration to within 10% of the value of the concentration predicted for the starting mix. We therefore quote an uncertainty of 10% associated with the erbium concentration in the single crystals.

The garnet crystal structure is cubic with a space group of Ia3d and 8 molecules per unit cell and a unit cell length of 12 Å. The majority of Er^{3+} ions substitute for Y^{3+} ions in D_2 sites during crystal growth. At the concentrations of Er^{3+} reported in this study, we observe no Er^{3+} spectra in interstitial or C_{3i} sites.

Absorption spectra were obtained between 200 and 1550 nm with a Cary Model 2390 spectrophotometer. Spectral bandwidths as narrow as 0.05 nm were required in certain cases for sharp peaks having

a bandwidth at half maximum of about 0.1 nm. Calibration tests of the instrument at a number of standards wavelengths indicated accuracy to within 0.1 nm over the entire wavelength range investigated. Absorption spectra obtained at wavelengths shorter than 280 nm, even at the lowest temperature investigated (nominally 4 K), were not sufficiently resolved to include in the intensity analysis. An analysis of the crystal-field splitting structure of the $Er^{3+}(4f^{11})$ spectra taken on the same samples that were used in the present study was reported earlier by Gruber et al.,[16] but their analysis did not include an intensity analysis of the individual transitions between the Stark levels.

Absorption spectra were also obtained on a second crystal having the same erbium concentration between 440 and 1550 nm with a Cary Model 14R spectrophotometer controlled by a desktop computer. The spectra were obtained at 0.1 nm intervals, and the spectral bandwidth was automatically maintained at about 0.05 nm for measurements at wavelengths shorter than 900 nm and about 0.1 nm for measurements above 1000 nm. Observed line widths are, with few exceptions, broader than the resolution of the spectrometers that recorded the data. Transitions from the ground-state Stark level to Stark levels in excited manifolds show well defined peak profiles from which line strength cross-sections were easily determined from a flat baseline. The line strengths, representing absorption transitions between individual Stark levels, were measured at about 12 K with the sample mounted on a cold finger of a CTI Model 22 closed cycle cryogenic refrigerator. Using the intensities of the first crystal as a standard, we compared individual line strengths to comparable transitions in the second crystal over the wavelength region of overlap between the two spectra, finding the match of intensities to be better than 10% between the two samples. This confirmed to within the stated uncertainty the erbium concentration for both crystals. By using the intensity measurements from both sets of data, we were able to expand the wavelength range of coverage and find supporting evidence for the individual line strength assignments. Accounting for the uncertainty in the Er^{3+} concentration in the two samples and the differences in the temperature between the two measurements, we estimate an overall maximum uncertainty in the experimental line strengths reported from both data sets to be less than 20%.

At the temperatures quoted for either sample (nominally 4 or 12 K), the first excited energy (Stark) level of the ground-state manifold of Er^{3+}, $^4I_{15/2}$, at 22 cm^{-1} is marginally populated. Representative of the 12 K spectrum, for example, are the absorption cross sections shown in Fig. 1 that represent transitions from $^4I_{15/2}$ to individual Stark levels in the $^4I_{13/2}$ manifold. In this figure, transitions from the excited Stark level at 22 cm^{-1} represent less than 10% of the intensity of the transitions from the ground-state Stark level to the 7 $(J + 1/2)$ Stark levels of the $^4I_{13/2}$ manifold. The percent contribution from observed hot bands to the total intensity of the absorption spectrum of $^2H(2)_{11/2}$ at 12 K as shown in Fig. 2 is even smaller, less than 5%. Both Figs. 1 and 2 represent the strongest manifold-to-manifold transitions observed in the Er^{3+} absorption spectrum. In the figures, the absorption cross sections are labeled according to their identification in Table 4. The hot-band transitions from the 22 cm^{-1} Stark level are labeled (H). The difference in line strengths between the 4 and 12 K absorption spectra represented by these two figures is less than 10%, a value within the uncertainty quoted earlier for the two sets of data.

Other excited manifolds, where the line strengths of the hot bands are 15% or less relative to the

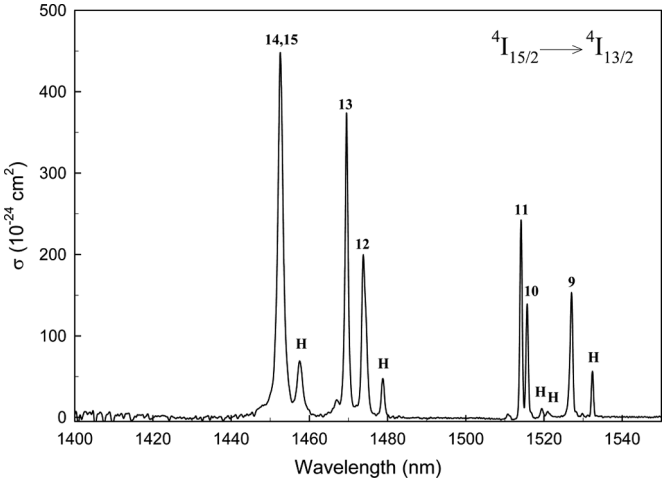

FIGURE 1 **Absorption spectrum from the ground state of $^4I_{15/2}$ to the $^4I_{13/2}$ manifold at approximately 12 K. Transition labels 9 through 15 identify final state energy levels given in Table 4. Hot-bands from the thermally populated level at 22 cm^{-1} are denoted by H.**

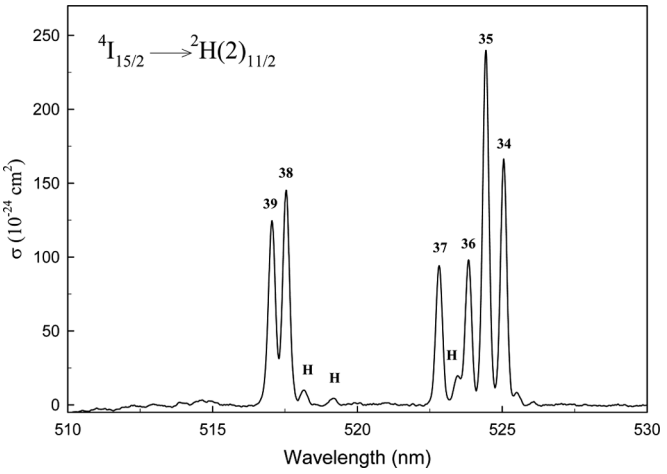

FIGURE 2 **Absorption spectrum from the ground state of $^4I_{15/2}$ to the $^2H(2)_{11/2}$ manifold at approximately 12 K, using the same notation as Fig. 1.**

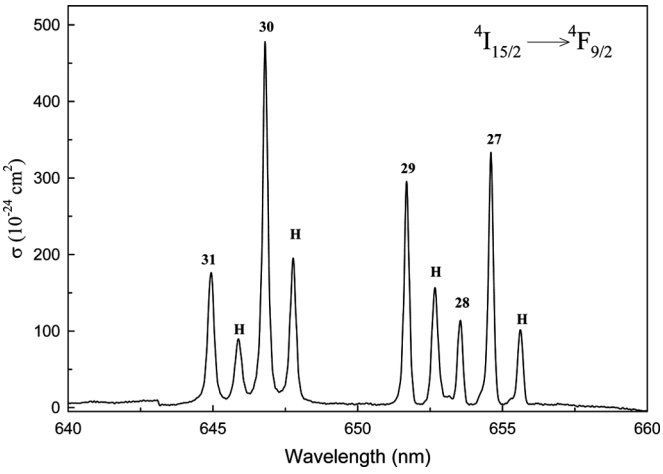

FIGURE 4 **Absorption spectrum from the ground state of $^4I_{15/2}$ to the $^4F_{9/2}$ manifold at approximately 12 K, using the same notation as Fig. 1.**

GSA include, $^4I_{11//2}$, $^4S_{3/2}$, $^4F_{5/2}$, $^4F_{7/2}$, $^4F_{3/2}$, $^4G_{11/2}$, $^4G_{9/2}$, $^2K_{15/2}$, $^2K_{13/2}$, $^2P_{3/2}$, $^2P_{1/2}$, $^4G_{5/2}$, $^2D(1)_{5/2}$, $^2H(2)_{9/2}$. We should point out here that for absorption at wavelengths shorter than 440 nm only the 4 K data were available for analysis. In several instances, the 12 K absorption spectrum of the $^4I_{9/2}$ and $^4F_{9/2}$ multiplet manifolds had hot-band absorption relative to the ground state absorption at significantly higher percentages than observed in the 4 K spectrum, as shown in Figs. 3 and 4. In these instances, we chose the 4 K cross sections where the percentage contribution was more in line with the other data taken at that temperature.

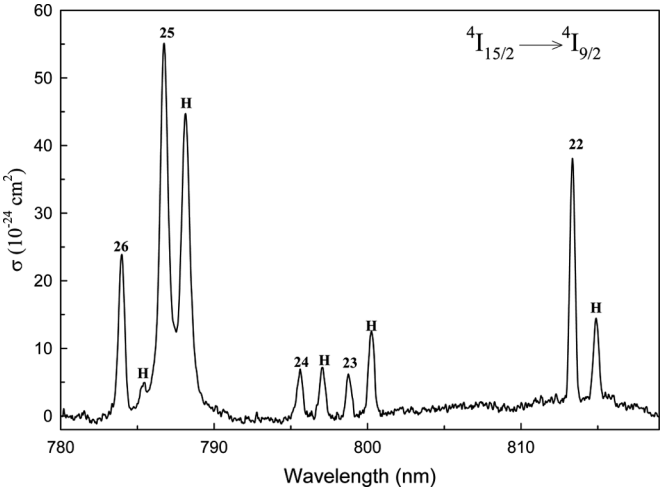

FIGURE 3 **Absorption spectrum from the ground state of $^4I_{15/2}$ to the $^4I_{9/2}$ manifold at approximately 12 K, using the same notation as Fig. 1.**

ENERGY LEVEL ANALYSIS

The 125 experimental energy levels analyzed in this study span 29 $^{2S+1}L_J$ multiplet manifolds up to 44,000 cm^{-1}. The electronic energy level structure of Er:YAG is analyzed by means of a model Hamiltonian defined to operate within the $4f^{11}$ electronic configuration of Er^{3+}. All parts of the Hamiltonian that depend upon 4f-electron radial coordinates or describe intermixing from excited configurations are represented as variable parameters. The model Hamiltonian is partitioned as,

$$\boldsymbol{H} = \boldsymbol{H}_{\mathrm{A}} + \boldsymbol{H}_{\mathrm{CF}} + \boldsymbol{H}_{\mathrm{CCF}} \tag{1}$$

where $\boldsymbol{H}_{\mathrm{A}}$ is the "atomic" Hamiltonian defined to include all relevant interactions except those associated with non-spherically symmetric components of the crystal field. The $\boldsymbol{H}_{\mathrm{CF}}$ and $\boldsymbol{H}_{\mathrm{CCF}}$ denote one-electron crystal-field and two-electron correlation-crystal-field interactions, respectively. The atomic Hamiltonian is expressed as,

$$\begin{aligned}\boldsymbol{H}_A = {} & E_{avg} + \sum_k F^k \boldsymbol{f}_k + \alpha \boldsymbol{L}(\boldsymbol{L}+1) \\ & + \beta \boldsymbol{G}(G_2) + \gamma \boldsymbol{G}(R_7) + \sum_i T^i \boldsymbol{t}_i + \varsigma_{so} \boldsymbol{A}_{so} \\ & + \sum_k P^k \boldsymbol{p}_k + \sum_j M^j \boldsymbol{m}_j \end{aligned} \tag{2}$$

where $k = 2, 4, 6$; $i = 2, 3, 4, 6, 7, 8$; and $j = 0, 2, 4$. The parameters and operators are defined according to standard practice.[19,20] Corrected values[21] for the

$\boldsymbol{p}_k$ and $\boldsymbol{m}_j$ operators have been used, which improves the standard deviation of the energy level fitting by about $2\,\mathrm{cm}^{-1}$.

The $\boldsymbol{H}_{\mathrm{CF}}$ Hamiltonian includes the non-spherically symmetric one-electron crystal-field interactions, and may be expressed in Wybourne notation as,

$$\boldsymbol{H}_{CF} = \sum_{k,q} B_q^k \boldsymbol{C}_q^{(k)} \tag{3}$$

where $k = 2$, 4, and 6; and $|q| \leq k$ is constrained by the site symmetry of the lanthanide ion. The B_q^k parameters contain the radially dependent parts of the one-electron crystal-field interactions and the $\boldsymbol{C}_q^{(k)}$ are many-electron spherical tensor operators acting within the $4f^N$ configuration. For D_2 site symmetry, q is restricted to 0, ±2, ±4, and ±6, and Eq. (3) may be expanded as,

$$\begin{aligned}\boldsymbol{H}_{\mathrm{CF}} = {} & B_0^2\boldsymbol{C}_0^{(2)} + B_2^2\left(\boldsymbol{C}_2^{(2)} + \boldsymbol{C}_{-2}^{(2)}\right) + B_0^4\boldsymbol{C}_0^{(4)} \\ & + B_2^4\left(\boldsymbol{C}_2^{(4)} + \boldsymbol{C}_{-2}^{(4)}\right) + B_4^4\left(\boldsymbol{C}_4^{(4)} + \boldsymbol{C}_{-4}^{(4)}\right) + B_0^6\boldsymbol{C}_0^{(6)} \\ & + B_2^6\left(\boldsymbol{C}_2^{(6)} + \boldsymbol{C}_{-2}^{(6)}\right) + B_4^6\left(\boldsymbol{C}_4^{(6)} + \boldsymbol{C}_{-4}^{(6)}\right) \\ & + B_6^6\left(\boldsymbol{C}_6^{(6)} + \boldsymbol{C}_{-6}^{(6)}\right)\end{aligned} \tag{4}$$

The $\boldsymbol{H}_{\mathrm{CCF}}$ Hamiltonian is defined to include contributions from two-electron correlation-crystal-field interactions according to the prescriptions of Judd[22] and Reid.[23] This Hamiltonian contains a large number of terms. However, previous studies have shown that Judd's simplified "delta-function" correlation-crystal-field operators[24] have been effective in explaining energy level anomalies in Pr^{3+},[25] and Nd^{3+}.[26] The delta-function CCF Hamiltonian may be represented as,

$$\boldsymbol{H}_{\mathrm{CCF}} = \sum_{k,q} D_q^k \delta_q^{(k)} \tag{5}$$

where $k \leq 12$ is restricted to the even integers and q is restricted by the site symmetry. In practice, we have found that contributions from $k > 6$ are not significant. When these terms are omitted, the allowed (k,q) values for the correlation-crystal-field D_q^k parameters exactly correspond to the allowed crystal-field B_q^k parameters. A further simplifying assumption that the q-dependence of the D_q^k scales with respect to the B_q^k, allows the following identification,

$$D_q^k = D_0^k\left(\frac{B_q^k}{B_0^k}\right) \tag{6}$$

reducing the number of independently fitted correlation-crystal-field parameters to three: D_0^2, D_0^4, and D_0^6.

Written in terms of the ortho-normalized $\boldsymbol{g}_{iq}^{(k)}$ correlation-crystal-field operators, the delta-function operators are given as,[27]

$$\delta_q^2 = \frac{35\sqrt{7}}{3\sqrt{2}}\boldsymbol{g}_{2q}^2 - \frac{35\sqrt{7}}{\sqrt{22}}\boldsymbol{g}_{3q}^2 - \frac{28\sqrt{105}}{\sqrt{143}}\boldsymbol{g}_{10q}^2 \tag{7}$$

$$\begin{aligned}\delta_q^4 = {} & -\frac{21\sqrt{105}}{2\sqrt{11}}\boldsymbol{g}_{2q}^4 + \frac{63\sqrt{105}}{22}\boldsymbol{g}_{3q}^4 + \frac{84\sqrt{42}}{\sqrt{715}}\boldsymbol{g}_{10\mathrm{A}q}^4 \\ & + \frac{8232\sqrt{3}}{11\sqrt{1105}}\boldsymbol{g}_{10\mathrm{B}q}^4\end{aligned} \tag{8}$$

$$\begin{aligned}\delta_q^6 = {} & \frac{35\sqrt{455}}{3\sqrt{22}}\boldsymbol{g}_{2q}^6 - \frac{35\sqrt{455}}{11\sqrt{2}}\boldsymbol{g}_{3q}^6 + \frac{56\sqrt{1365}}{\sqrt{6479}}\boldsymbol{g}_{10\mathrm{A}q}^6 \\ & + \frac{588\sqrt{65}}{11\sqrt{527}}\boldsymbol{g}_{10\mathrm{B}q}^6\end{aligned} \tag{9}$$

It is well understood that for lanthanide systems having low site symmetry, different possible orientations of the crystal-field quantization axes will result in different parameter sets that yield identical calculated energy levels.[28,29] For D_2 symmetry, such as the Er:YAG system examined here, there are three inequivalent orthogonal C_2 symmetry axes, typically labeled as the crystallographic *a, b*, and *c* axes. This allows three different orientations of the quantization *z*-axis parallel to a C_2 symmetry axis. For each of these three *z*-axis orientations, there exist two orientations of the *x* and *y* axes along the two remaining C_2 symmetry axes, resulting in six alternative sets of crystal-field parameters for which only the nine crystal-field parameters of Eq. (4) are non-zero.[30] The *z, x*, and *y* axes determined here correspond to the six possible permutations of the orthogonal crystallographic *a, b*, and *c* axes. However, it is not possible from the isotropic data presented here to uniquely identify which parameterization corresponds to which permutation of the crystallographic axes.

Transformations between these six equivalent parameter sets involve 90 degree rotations about

the x, y, and z axes, and have been investigated by Morrison and Leavitt,[15] and Rudowicz and Bramley.[31] The transformation equations given on page 633 of Ref.[15] correspond to the S6 transformation of Rudowicz and Bramley, which is a 90 degree rotation about the y-axis, though it should be noted that the minus sign in the expression for $\boldsymbol{B}'_{22}$ of Ref.[15] is a misprint. This transformation converts between the following pairs of parameter sets (the transformation is its own inverse, as parameters in D_2 symmetry are invariant with respect to 180° rotation): Set 1 (upper sign) to Set 2 (upper sign), Set 2 (lower sign) to Set 3 (lower sign), and Set 1 (lower sign) to Set 3 (upper sign). Changing signs on the $q = 2, 6$ terms converts between the upper sign and the lower sign parameters of each set, and corresponds to the S3 transformation of Rudowicz and Bramley, which is a 90° rotation about the z-axis. These transformations provide an effective way to determine the other five equivalent parameter sets once an initial set is realized.

For the purposes of this work, we use a modified Morrison and Leavitt notation, where the signs on the $q = 2, 6$ terms of Set 2 are reversed. This allows previously unrealized symmetries of the Morrison and Leavitt parameter sets to become apparent. Denoting the parameter set realized by the upper sign on the $q = 2, 6$ terms "a" and the parameter set realized by the lower signs "b", the 90° rotation about the y-axis (S6) converts between the following pairs of sets: $1a \leftrightarrow 2b$, $2a \leftrightarrow 3b$, and $3a \leftrightarrow 1b$. Additionally, a 120° rotation about the [111] axis (Rudowicz and Bramley[31] transformation S4) sequentially converts between each of the upper sign parameter sets: $1a \rightarrow 2a \rightarrow 3a \rightarrow 1a$, and between each of the lower sign parameter sets: $1b \rightarrow 3b \rightarrow 2b \rightarrow 1b$.

Crystal-field energy level parameters were determined using a Monte-Carlo method of random starting parameters[32,33] that was originally developed for determination of intensity parameters. Using this method, each of the nine crystal-field parameters are randomly varied between $\pm 1500\,\mathrm{cm}^{-1}$ to create multiple sets of starting parameters. Each of these starting parameter sets are optimized using a standard least-squares fitting between experimental and calculated energy levels. When many of these calculations are done, the local minima on the parameter error space are mapped out, along with the six-fold global minimum. Each local minimum also has a six-fold solution, and represents a different ordering of the Stark component energy level states. Once each minimum is determined, the correlation-crystal-field parameters are added and each minimum is refit with the ratios of the correlation-crystal-field parameters $\boldsymbol{D}_q^4/\boldsymbol{D}_0^4$ and $\boldsymbol{D}_q^6/\boldsymbol{D}_0^6$ held fixed at the crystal-field parameter ratios.

Table 1 presents the Hamiltonian parameters (in cm^{-1}) for the best-fit analysis of 125 experimentally determined energy levels. The left two columns of this table give the atomic parameters defined by Eq. (2) with statistical uncertainties given in parenthesis after the parameter values. Sixteen of the 20 atomic parameters were freely fit, the remaining four (M^2, M^4, P^4, P^6) were constrained by Hartree-Fock determined fixed ratios.

The six different sets of crystal-field parameters corresponding to the six axes orientations are presented in the three right-hand columns of Table 1, identified as Sets 1–3 in modified Morrison and Leavitt notation. Each column presents two possible sets of parameter values, indicated by the top and bottom symbols of the ± signs on the $q = 2, 6$ parameters. Values of the correlation-crystal-field delta-function parameters D^4 and D^6 are also presented in the three right-hand columns of Table 1, with parameter ratios held fixed at crystal-field-parameter ratios, as given by Eq. (6). The rank-two parameter D^2 did not have a statistically significant influence on the energy level fitting, and has therefore been removed from the fitting presented in Table 1. The standard deviation of the fitted energy levels with respect to experimentally determined values is $12.66\,\mathrm{cm}^{-1}$, or an r.m.s. error of $11.21\,\mathrm{cm}^{-1}$, compared to the r.m.s. deviation of $13.20\,\mathrm{cm}^{-1}$ reported by Gruber et al.[16] This fitting improvement is predominately due to two factors, the improved correlation-crystal-field parametrization from using the delta-function model rather than the previous arbitrary choice of a single parameter ($G^4_{10\mathrm{A}}$), and the corrected atomic operators $\boldsymbol{m}_j$ and $\boldsymbol{p}_k$.[21]

Our method of random starting parameters confirms that this is the best fit minimum, with the second-best minimum having a standard deviation of $14.43\,\mathrm{cm}^{-1}$, which is about 15% higher than the global minimum. This provides some evidence that the best fit minimum is the true global minimum.

In identifying which set of parameters corresponds to each of the Morrison and Leavitt sets, we

TABLE 1 Atomic and Crystal-Field Energy Parameters (in cm^{-1}) for Er:YAG. Six Alternative Crystal-Field parameter Sets are Presented Using Modified Morrison and Leavitt Notation, Together with Rotationally Invariant Crystal-Field Interaction Strengths

Atomic parameter	Value	Crystal-field parameter	Value		
			Set 1	Set 2	Set 3
E_{avg}	35652 (12)	B_0^2	341 (15)	102 (17)	−443 (14)
F^2	95683 (143)	B_2^2	±223 (11)	±320 (10)	±97 (12)
F^4	66691 (373)	B_0^4	−173 (51)	678 (58)	−1687 (47)
F^6	55533 (502)	B_2^4	±1496 (28)	±958 (31)	±538 (39)
α	17.1 (0.2)	B_4^4	−420 (41)	−1132 (33)	847 (33)
β	−606 (9)	B_0^6	−1178 (41)	−628 (52)	623 (46)
γ	1875 (116)	B_2^6	±323 (32)	±422 (40)	±152 (46)
ζ	2372 (2)	B_4^6	529 (28)	676 (31)	1010 (24)
T^2	601 (32)	B_6^6	±441 (46)	±664 (30)	±187 (32)
T^3	42 (3)	D_0^4	1.6 (0.2)	−6.2 (0.7)	15.4 (1.7)
T^4	61 (4)	D_2^4	[±13.7]	[±8.8]	[±4.9]
T^6	−375 (9)	D_4^4	[3.9]	[10.4]	[−7.8]
T^7	318 (20)	D_0^6	−7.0 (1.8)	−3.8 (1.0)	3.7 (0.9)
T^8	593 (29)	D_2^6	[±1.9]	[±2.5]	[∓0.9]
M^0	3.9 (0.2)	D_4^6	[3.2]	[4.0]	[6.0]
M^2	$0.56M^0$	D_6^6	[±2.6]	[±4.0]	[∓1.1]
M^4	$0.38M^0$				
P^2	607 (52)	S_{cf}^2	208	208	208
P^4	$0.75P^2$	S_{cf}^4	735	735	735
P^6	$0.50P^2$	S_{cf}^6	442	442	442
		S_{ccf}^4	755	755	755
		S_{ccf}^6	331	331	331

have used a "closeness" criterion that minimizes the root mean square differences between the six sets of calculated crystal-field parameters and the parameters identified as Sets 1 to 3 by Morrison and Leavitt for Nd:YAG.[15] Results are presented in Table 2, where the r.m.s. differences between the six parameter sets of Table 1 and the Nd:YAG parameters Sets 1 to 3 of Morrison and Leavitt are given. The sets "*a*" use the upper signs on the $q = 2, 6$ parameters and the sets "*b*" use the lower signs. (Note that we identify the lower sign used by Morrison and Leavitt for Set 2 as "2*a*" and the upper sign as "2*b*" in order to take advantage of the transformation symmetries illustrated above; thus the "modified" Morrison and Leavitt notation.) As can be seen from Table 2, the smallest differences are on the diagonal entries, confirming the correspondence between parameter sets. These assignments

TABLE 2 Root-Mean-Square Distances (in cm^{-1}) between the Calculated Crystal Field Parameter Sets of Table 1 for Er:YAG and the Morrison and Leavitt Sets 1 to 3 (Upper and Lower Signs) Published for Nd:YAG.[15] Sets "*a*" ("*b*") Refer to the Upper (Lower) Signs on the $q = 2, 6$ Parameters Using Modified Morrison and Leavitt Notation

Morrison & Leavitt Nd:YAG Set	Er:YAG set					
	1*a*	1*b*	2*a*	2*b*	3*a*	3*b*
1-upper	**380**	1435	1344	579	1387	1220
1-lower	1435	**380**	579	1344	1220	1387
2-lower*	1387	579	**380**	1220	1344	1435
2-upper*	579	1387	1220	**380**	1435	1344
3-upper	1344	1220	1387	1435	**380**	579
3-lower	1220	1344	1435	1387	579	**380**

*Modified Morrison & Leavitt notation reverses the upper and lower signs on the Set 2 parameters in order to take advantage of transformation symmetries (see text).

are confirmed by verifying that the identified parameter sets satisfy the transformation relationships between parameter sets given above. Use of this closeness criterion allows the dominant rank 4 and 6 parameters to determine the identification of each set, and is consistent with observed parameter trends. In particular, it is well-recognized in the literature that the rank 4 and 6 parameters of Set 3 are dominated by the $q = 0$, 4 terms, representing the approximate D_{2d} symmetry of the YAG system. Sets 1 and 2 are best distinguished by the rank 4 terms, with Set 1 being dominated by the $\boldsymbol{B}_2^4$ term whereas Set 2 has roughly equivalent $\boldsymbol{B}_2^4$ and $\boldsymbol{B}_4^4$ terms.

The Set 1*a* parameters presented in Table 1 are similar to those previously reported by Gruber et al.[16] Converted from unit-tensor to spherical-tensor notation, their crystal-field parameters become: $\boldsymbol{B}_0^2 = 326$, $\boldsymbol{B}_2^2 = 227$, $\boldsymbol{B}_0^4 = -199$, $\boldsymbol{B}_2^4 = -1590$, $\boldsymbol{B}_4^4 = -449$, $\boldsymbol{B}_0^6 = -1164$, $\boldsymbol{B}_2^6 = -283$, $\boldsymbol{B}_4^6 = 496$, and $\boldsymbol{B}_6^6 = -402\,\mathrm{cm}^{-1}$.

Interestingly, the Set 3*b* parameters represent the "standardized" parameter set of Rudowicz,[34] based on the rhombicity ratio $\kappa = \boldsymbol{B}_2^2/\boldsymbol{B}_0^2$ being in the "standard" range $(0, \sqrt{6})$, even though the original Morrison and Leavitt parameters for Nd:YAG used to define Sets 1 to 3 have Set 1*a* in standardized notation. As can be seen from the $1220\,\mathrm{cm}^{-1}$ entry in the first row of the 3*b* column, these two "standardized" parameter sets are far from similar. In order to examine the source of this anomaly, we have calculated the angle between the crystal-field tensors of the each rank for the Nd:YAG parameters of Morrison and Leavitt[15] and the calculated Er:YAG parameters, using the equation,

$$\cos(\theta_k) = \frac{\mathbf{B}^{(k)}(Er) \circ \mathbf{B}^{(k)}(Nd)}{|\mathbf{B}^{(k)}(Er)||\mathbf{B}^{(k)}(Nd)|} = \frac{B_0^k(Er) \cdot B_0^k(Nd) + 2\sum_{q>0} B_q^k(Er) \cdot B_q^k(Nd)}{\sqrt{\left(B_0^k(Er)\right)^2 + 2\sum_{q>0}\left(B_q^k(Er)\right)^2}\sqrt{\left(B_0^k(Nd)\right)^2 + 2\sum_{q>0}\left(B_q^k(Nd)\right)^2}} \tag{10}$$

TABLE 3 **Vector Angles (in Degrees) for Rank 2, 4, and 6 Crystal-Field Parameter Tensors between the Calculated Sets of Table 1 for Er:YAG and the Morrison and Leavitt Sets 1 to 3 Published for Nd:YAG.[15] Sets "*a*" ("*b*") Refer to the Upper (Lower) Signs on the $q = 2$, 6 Parameters Using Modified Morrison and Leavitt Notation**

Morrison & Leavitt Nd:YAG Set	Er:YAG set					
	1*a*	1*b*	2*a*	2*b*	3*a*	3*b*
Rank = 2						
1*a*	**23.2**	62.3	96.8	57.7	143.2	177.7
1*b*	62.3	**23.2**	57.7	96.8	177.7	143.2
2*a*	143.2	57.7	**23.2**	177.7	96.8	62.3
2*b*	57.7	143.2	177.7	**23.2**	62.3	96.8
3*a*	96.8	177.7	143.2	62.3	**23.2**	57.7
3*b*	177.7	96.8	62.3	143.2	57.7	**23.2**
Rank = 4						
1*a*	**9.8**	137.5	106.2	34.4	116.9	80.4
1*b*	137.5	**9.8**	34.4	106.2	80.4	116.9
2*a*	116.9	34.4	**9.8**	80.4	106.2	137.5
2*b*	34.4	116.9	80.4	**9.8**	137.5	106.2
3*a*	106.2	80.4	116.9	137.5	**9.8**	34.4
3*b*	80.4	106.2	137.5	116.9	34.4	**9.8**
Rank = 6						
1*a*	**8.9**	64.3	81.5	20.9	73.8	88.2
1*b*	64.3	**8.9**	20.9	81.5	88.2	73.8
2*a*	73.8	20.9	**8.9**	88.2	81.5	64.3
2*b*	20.9	73.8	88.2	**8.9**	64.3	81.5
3*a*	81.5	88.2	73.8	64.3	**8.9**	20.9
3*b*	88.2	81.5	64.3	73.8	20.9	**8.9**

TABLE 4 Calculated and Experimentally Observed Energy Levels and Transition Line Strengths for Er^{3+}: YAG

		M_J (largest component)			Energy (cm^{-1})			Line strengths ($10^{-24}\,cm^2$)		
Multiplet	Level	Set 1	Set 2	Set 3	E_{exp}	E_{calc}	ΔE	Exp	Calc	(E − C)/E
$^4I_{15/2}$	1	±7/2	±5/2	±13/2	0	–7	7			
	2	±5/2	±7/2	±15/2	22	12	10			
	3	±15/2	±9/2	±1/2	60	52	8			
	4	±9/2	±11/2	±1/2	80	91	–11			
	5	±3/2	±13/2	±9/2	417	401	16			
	6	±1/2	±15/2	±11/2	432	434	–2			
	7	±11/2	±1/2	±9/2		512				
	8	±13/2	±3/2	±7/2	574	573	1			
$^4I_{13/2}$	9	±3/2	±3/2	±13/2	6549	6542	7	118	100	0.155
	10	±13/2	±7/2	±3/2	6599	6596	3	107	122	–0.138
	11	±7/2	±9/2	±1/2	6606	6606	0	169	104	0.382
	12	±5/2	±11/2	±5/2	6786	6771	15	155	197	–0.268
	13	±1/2	±13/2	±5/2	6805	6821	–16	291	283	0.026
	14	±9/2	±1/2	±7/2	6883	6877	6	30.2	33.9	–0.122
	15	±11/2	±3/2	±7/2	6889	6887	2	91.1	60.6	0.335
$^4I_{11/2}$	16	±3/2	±5/2	±11/2	10255	10255	0	161	138	0.141
	17	±7/2	±7/2	±1/2	10285	10293	–8	43.2	18.7	0.567
	18	±5/2	±9/2	±3/2	10361	10361	0	11.3	13.6	–0.205
	19	±1/2	±11/2	±9/2	10372	10388	–16	91.1	51.1	0.439
	20	±9/2	±1/2	±7/2	10412	10421	–9	70.7	69.6	0.015
	21	±11/2	±3/2	±5/2	10417	10425	–8	70.7	70.7	–0.000
$^4I_{9/2}$	22	±5/2	±5/2	±1/2	12297	12301	–4	32.6	21.3	0.346
	23	±3/2	±7/2	±7/2	12522	12522	0	7.82	9.00	–0.151
	24	±9/2	±3/2	±3/2	12572	12570	2	8.02	7.67	0.043
	25	±1/2	±1/2	±9/2	12714	12717	–3	45.9	58.1	–0.265
	26	±7/2	±7/2	±5/2	12759	12761	–2	21.4	7.92	0.630
$^4F_{9/2}$	27	±9/2	±7/2	±1/2	15288	15297	–9	264	239	0.094
	28	±7/2	±5/2	±1/2	15312	15329	–17	92.7	83.2	0.103
	29	±1/2	±3/2	±9/2	15357	15380	–23	232	9.13	0.961
	30	±3/2	±9/2	±5/2	15473	15479	–6	376	53.1	0.859
	31	±5/2	±3/2	±7/2	15518	15510	8	141	94.9	0.327
$^4S_{3/2}$	32	±3/2	±3/2	±1/2	18394	18397	–3	104	65.7	0.368
	33	±1/2	±1/2	±3/2	18459	18455	4	135	180	–0.337
$^2H(2)_{11/2}$	34	±7/2	±1/2	±9/2	19094	19118	–24	129	113	0.126
	35	±5/2	±5/2	±7/2	19114	19136	–22	185	238	–0.285
	36	±3/2	±11/2	±5/2	19152	19162	–10	76.0	86.3	–0.136
	37	±9/2	±9/2	±3/2	19348	19325	23	72.2	65.8	0.088
	38	±1/2	±5/2	±11/2	19366	19341	25	113	104	0.079
	39	±11/2	±7/2	±1/2	19370	19354	16	96.9	106	–0.091
$^4F_{7/2}$	40	±3/2	±7/2	±5/2	20514	20513	1	34.4	31.7	0.079
	41	±7/2	±3/2	±1/2	20570	20551	19	12.3	13.8	–0.118
	42	±5/2	±5/2	±3/2	20650	20646	4	29.1	38.9	–0.338
	43	±1/2	±1/2	±7/2	20701	20695	6	20.5	18.6	0.095
$^4F_{5/2}$	44	±3/2	±5/2	±3/2	22224	22222	2	15.4	15.3	0.009
	45	±5/2	±1/2	±1/2	22244	22243	1	92.7	58.6	0.368
	46	±1/2	±3/2	±5/2	22291	22295	–4	13.2	13.0	0.015
$^4F_{3/2}$	47	±3/2	±1/2	±1/2	22595	22609	–14	43.7	37.1	0.150
	48	±1/2	±3/2	±3/2	22666	22661	5	59.5	60.2	–0.012
$^2G(1)_{9/2}$	49	±5/2	±5/2	±1/2	22423	24405	18	68.4	43.9	0.358
	50	±3/2	±7/2	±7/2	24577	24565	12	13.9	16.5	–0.189

(*Continued*)

TABLE 4 Continued

Multiplet	Level	M_J (largest component)			Energy (cm^{-1})			Line strengths ($10^{-24}\,cm^2$)		
		Set 1	Set 2	Set 3	E_{exp}	E_{calc}	ΔE	Exp	Calc	(E − C)/E
	51	±9/2	±3/2	±3/2	24593	24584	9	21.9	20.9	0.046
	52	±1/2	±1/2	±9/2	24765	24752	13	2.76	3.16	–0.143
	53	±7/2	±7/2	±5/2	24785	24777	8	2.57	3.16	–0.231
$^4G_{11/2}$	54	±7/2	±1/2	±7/2	26215	26237	–22	323	194	0.399
	55	±5/2	±3/2	±5/2	26277	26283	–6	267	237	0.112
	56	±3/2	±5/2	±9/2	26323	26327	–4	57.0	63.9	–0.121
	57	±9/2	±7/2	±3/2	26567	26574	–7	36.7	34.8	0.052
	58	±7/2	±5/2	±1/2	26574	26592	–18	498	343	0.311
	59	±1/2	±1/2	±11/2	26605	26614	–9	138	121	0.125
$^2K_{15/2}$	60	±1/2	±1/2	±15/2	27298	27287	11	6.88	6.66	0.032
$^4G_{9/2}$	61	±1/2	±9/2	±5/2	27322	27322	0	17.4	20.2	–0.160
$^4G_{9/2}$	62	±3/2	±3/2	±7/2	27368	27340	28	16.3	9.71	0.404
$^4G_{9/2}$	63	±7/2	±7/2	±3/2	27486	27481	5	58.0	40.5	0.302
$^4G_{9/2}$	64	±1/2	±1/2	±9/2	27498	27493	5	99.3	83.8	0.156
$^4G_{9/2}$	65	±5/2	±5/2	±1/2	27531	27523	8	0.258	0.261	–0.011
$^2K_{15/2}$	66	±11/2	±9/2	±3/2	27585	27583	2	2.66	2.60	0.022
$^2K_{15/2}$	67	±13/2	±11/2	±1/2	27596	27597	–1	0.778	0.871	–0.119
$^2K_{15/2}$	68	±5/2	±7/2	±13/2	27741	27741	0	6.24	6.36	0.019
$^2K_{15/2}$	69	±7/2	±13/2	±5/2	27860	27865	–5	7.42	8.37	–0.128
$^2K_{15/2}$	70	±1/2	±15/2	±7/2	27920	27923	–3	0.772	0.848	0.099
$^2K_{15/2}$	71	±13/2	±3/2	±9/2	27980	27997	–17	10.3	10.4	–0.010
$^2K_{15/2}$	72	±15/2	±1/2	±11/2	28042	28034	8	14.8	15.3	–0.031
$^4G_{7/2}$	73	±3/2	±3/2	±1/2	28070	28085	–15	39.2	37.5	0.044
$^2K_{15/2}$	74	±11/2	±1/2	±9/2	28117	28101	16	0.894	0.856	0.042
$^4G_{7/2}$	75	±5/2	±5/2	±3/2	28150	28151	–1	58.9	53.6	0.091
$^4G_{7/2}$	76	±1/2	±1/2	±7/2	28166	28165	1	15.6	14.9	0.043
$^2P_{3/2}$	77	±3/2	±3/2	±1/2	31480	31507	–27	6.53	6.65	–0.019
	78	±1/2	±1/2	±3/2	31600	31597	3	12.2	12.3	–0.006
$^2K_{13/2}$	79	±1/2	±1/2	±13/2	32600	32602	–2	0.264	0.251	0.051
$^2K_{13/2}$	80	±7/2	±9/2	±1/2	32814	32832	–18	0.366	0.375	–0.024
$^2K_{13/2}$	81	±9/2	±11/2	±3/2	32855	32840	15	0.123	0.121	0.014
$^2K_{13/2}$	82	±5/2	±11/2	±11/2	33006	33002	4	3.54	3.60	–0.018
$^2P_{1/2}$	83	±1/2	±1/2	±1/2	33026	33021	5	0.152	0.133	0.126
$^4G_{5/2}$	84	±5/2	±1/2	±3/2	33085	33072	13	0.705	0.716	–0.016
$^2K_{13/2}$	85	±1/2	±13/2	±5/2	33166	33175	–9	2.44	2.45	–0.003
$^2K_{13/2}$	86	±11/2	±3/2	±9/2	33246	33242	4	0.960	0.969	–0.010
$^2K_{13/2}$	87	±13/2	±1/2	±9/2	33318	33317	1	1.15	1.17	–0.015
$^4G_{5/2}$	88	±3/2	±1/2	±1/2	33338	33344	–5	1.12	1.06	0.052
$^4G_{5/2}$	89	±1/2	±3/2	±1/2	33469	33467	2	0.413	0.392	0.050
$^4G_{7/2}$	90	±5/2	±7/2	±3/2	34014	34008	6	10.3	10.1	0.025
	91	±7/2	±3/2	±5/2	34030	34041	–11	1.50	1.41	0.060
	92	±1/2	±7/2	±1/2	34097	34067	30	1.88	3.16	–0.681
	93	±3/2	±3/2	±7/2	34172	34199	–27	26.4	24.8	0.062
$^2D(1)_{5/2}$	94	±5/2	±3/2	±1/2	34750	34748	2	1.56	1.45	0.070
	95	±3/2	±1/2	±5/2	34792	34796	–4	4.41	4.31	0.023
	96	±1/2	±5/2	±3/2	34897	34895	2	2.38	2.41	–0.013
$^2H(2)_{9/2}$	97	±7/2	±7/2	±5/2	36332	36336	–4		0.957	
	98	±1/2	±1/2	±1/2	36400	36407	–7		21.8	
	99	±9/2	±9/2	±3/2	36504	36501	3		1.34	
	100	±3/2	±7/2	±7/2	36586	36579	7		2.60	

(*Continued*)

TABLE 4 Continued

Multiplet	Level	M_J (largest component)			Energy (cm^{-1})			Line strengths ($10^{-24}\,cm^2$)		
		Set 1	Set 2	Set 3	E_{exp}	E_{calc}	ΔE	Exp	Calc	(E − C)/E
	101	±5/2	±5/2	±1/2	36813	36817	–4		3.64	
$^4D_{5/2}$	102	±5/2	±3/2	±1/2	38500	38503	–3		1.85	
	103	±3/2	±5/2	±3/2	38535	38543	–8		4.42	
	104	±1/2	±1/2	±5/2	38570	38560	10		5.56	
$^4D_{7/2}$	105	±1/2	±3/2	±7/2	39020	39036	–16		752	
	106	±3/2	±1/2	±5/2	39065	39065	0		129	
	107	±5/2	±7/2	±3/2		39190			50.5	
	108	±7/2	±3/2	±1/2	39360	39349	11		96.7	
$^2I_{11/2}$	109	±9/2	±3/2	±11/2	40871	40886	–15		5.43	
$^2I_{11/2}$*	110	±3/2	±1/2	±17/2	40938	40932	6		2.02	
$^2I_{11/2}$	111	±1/2	±7/2	±7/2	40968	40945	23		7.93	
$^2I_{11/2}$	112	±7/2	±9/2	±5/2	41006	41002	4		1.16	
$^2I_{11/2}$*	113	±3/2	±11/2	±17/2		41094			5.57	
$^2I_{11/2}$	114	±5/2	±3/2	±3/2	41138	41153	–15		1.50	
$^2I_{11/2}$	115	±7/2	±7/2	±1/2	41206	41219	–13		5.41	
$^2L_{17/2}$	116	±3/2	±7/2	±15/2	41318	41327	–9		12.6	
$^2L_{17/2}$	117	±7/2	±13/2	±13/2		41440			0.975	
$^2L_{17/2}$	118	±13/2	±13/2	±1/2	41500	41495	5		14.8	
$^2L_{17/2}$	119	±13/2	±5/2	±11/2		41522			15.2	
$^2L_{17/2}$	120	±11/2	±11/2	±3/2	41546	41540	6		11.5	
$^2L_{17/2}$	121	±15/2	±7/2	±9/2	41571	41581	–10		0.012	
$^2L_{17/2}$	122	±7/2	±17/2	±7/2	41622	41618	4		1.65	
$^2L_{17/2}$	123	±17/2	±1/2	±5/2	41730	41733	–3		5.24	
$^4D_{3/2}$	124	±3/2	±3/2	±1/2	42208	42205	3		4.34	
	125	±1/2	±1/2	±3/2	42260	42251	9		4.96	
$^2P_{3/2}$	126	±1/2	±1/2	±3/2	42759	42756	3		0.031	
	127	±3/2	±3/2	±1/2	42804	42808	–4		0.048	
$^2I_{13/2}$	128	±11/2	±1/2	±9/2	43310	43317	–7		1.33	
	129	±9/2	±3/2	±11/2		43348			3.96	
	130	±1/2	±13/2	±5/2	43414	43403	11		2.10	
	131	±3/2	±11/2	±7/2	43465	43450	15		5.91	
	132	±5/2	±5/2	±13/2		43644			1.00	
	133	±7/2	±9/2	±3/2		43709			0.182	
	134	±13/2	±7/2	±1/2		43855			0.226	
$^4D_{1/2}$	135	±1/2	±1/2	±1/2		46942			0.362	
$^2L_{15/2}$	136	±1/2	±1/2	±15/2		47216			1.44	
	137	±9/2	±13/2	±5/2		47469			0.596	
	138	±5/2	±9/2	±13/2		47553			0.428	
	139	±7/2	±11/2	±11/2		47602			0.657	
	140	±11/2	±7/2	±1/2		47687			0.663	
	141	±3/2	±15/2	±9/2		47704			0.036	
	142	±13/2	±15/2	±7/2		47779			0.148	
	143	±15/2	±1/2	±5/2		47912			0.174	
$^2H(2)_{11/2}$	144	±1/2	±1/2	±9/2		48016			0.564	
	145	±7/2	±7/2	±5/2		48063			0.253	
	146	±5/2	±3/2	±7/2		48139			0.117	
	147	±3/2	±9/2	±3/2		48182			0.065	
	148	±9/2	±5/2	±1/2		48351			0.115	
$^2D(2)_{5/2}$	149	±1/2	±3/2	±5/2		48676			0.355	
	150	±5/2	±1/2	±1/2		48839			2.81	
	151	±3/2	±3/2	±3/2		48922			0.500	

*Largest component for levels 110 and 113 is $^2I_{11/2}$ for Sets 1 and 2, $^2L_{17/2}$ for Set 3.

where the number 2 in front of the summations accounts for the $q<0$ crystal-field terms included in Eq. (3). The $\cos(\theta_k)$ in Eq. (10) correspond to the "closeness factors" C_k of Rudowicz and Qin[28] and range from +1 (highly correlated) to −1 (highly anti-correlated), with 0 being completely uncorrelated. Angles in degrees, defined by Eq. (10), are tabulated in the three panels of Table 3 for the rank 2, 4, and 6 crystal-field parameters, respectively. As can be seen from the first row of the first panel, the rank 2 parameters in "standardized" notation (1*a* for Nd:YAG/3*b* for Er:YAG) are nearly antiparallel, at 177.7°. This indicates the nearly identical rhombicity ratios for these two standardized parameter sets, $\kappa(\mathrm{Nd}) = 129/514 = 0.25$ and $\kappa(\mathrm{Er}) = -97/-443 = 0.22$. However, as can be seen from the second and third panels, the rank 4 and 6 parameter sets are nearly completely uncorrelated, with an angle of 80.4° for the rank 4 tensors, and 88.2° for the rank 6 tensors. By contrast, the corresponding Morrison and Leavitt parameter sets are very well correlated, with the angles between rank 4 tensors at 9.8°, and rank 6 tensors at 8.9°. Corresponding parameter sets have a somewhat lesser correlation of rank 2 tensors, at 23.2°.

This illustrates a fundamental limitation of any standardization process that considers only rank 2 contributions. For YAG systems, the rank 2 terms are less well defined and have greater variability than the dominant rank 4 and 6 terms. Thus, enforcing a standardization based exclusively upon rank 2 terms will result in the dominant rank 4 and 6 terms having different, incommensurate parameter values, even if their parameters started out (prior to standardization) being nearly identical.

The relative strengths of crystal-field interactions for lanthanide ions in different site symmetries and in different host materials may be compared in terms of crystal-field strength parameters defined by[35,36]

$$S_{\mathrm{cf}}^{k} = \sqrt{\frac{1}{2k+1}\left[\left(B_0^k\right)^2 + 2\sum_{q>0}\left|B_q^k\right|^2\right]} \qquad (11)$$

where $k = 2$, 4, and 6. These crystal-field strength parameters are rotational invariants of the system, and thus independent of parametrization coordinates used.[37] As given in Table 1, the crystal-field strengths for Er:YAG are, $S_{\mathrm{cf}}^2 = 208$, $S_{\mathrm{cf}}^4 = 735$, and $S_{\mathrm{cf}}^6 = 442\,\mathrm{cm}^{-1}$.

Similarly, correlation-crystal-field interaction strength parameters are defined by[26]

$$S_{\mathrm{ccf}}^{k} = \left(\frac{N-1}{2\sqrt{6}}\right) \times \sqrt{\frac{1}{2k+1}\frac{1}{\langle f\|\boldsymbol{C}^{(k)}\|f\rangle^2}\sum_i\left[\left(G_{i0}^k\right)^2 + 2\sum_{q>0}\left|G_{iq}^k\right|^2\right]} \qquad (12)$$

where the initial multiplicative factor, dependent upon the number of electrons, accounts for the normalization difference between the one-body $\mathbf{U}^{(k)}$ operators (normalized to one in f^1) and two-body $\mathbf{g}^{(k)}$ operators (normalized to one in f^2).[23] The $\boldsymbol{C}^{(k)}$ factors account for the fact that the crystal-field parameters are defined in terms of spherical-tensor normalization. The correlation-crystal-field strengths, given in Table 1, are $S_{\mathrm{ccf}}^4 = 755$ and $S_{\mathrm{ccf}}^6 = 331\,\mathrm{cm}^{-1}$, which are comparable in magnitude to the crystal-field strengths.

Table 4 presents experimental and calculated energy levels for all states up to $50{,}000\,\mathrm{cm}^{-1}$. Each $4f^{11}$ energy level is a Kramer's doublet in D_2 symmetry, with irreps $\Gamma_{1/2}$ and $\Gamma_{3/2}$. The largest M_J components of each doublet are given in Table 4 for each of the three parameterization Sets 1, 2, and 3. As can be seen from this table, the largest M_J components of the ground state doublet are ±7/2, ±5/2, and ±13/2, respectively for Set 1, 2, and 3 parameterizations. Although these three sets are optically indistinguishable, the different M_J components should make these three orientations magnetically distinct. But this is beyond the scope of the current paper.

INTENSITY ANALYSIS

The 88 ground state absorption line strengths measured for 19 $^{2S+1}L_J$ multiplet manifolds between 6500 and $35{,}000\,\mathrm{cm}^{-1}$ are presented in the final three columns of Table 4, along with calculated line strengths and relative errors $(E_i - C_i)/E_i$. Experimental and calculated transition line strengths are given in units of $10^{-24}\,\mathrm{cm}^2$; relative errors are unitless.

Following the notation of Reid and Richardson,[38,39] transition line strengths are calculated by evaluating,

$$S_{i\to f}=e^2\left|\sum_{\lambda tp}A^{\lambda}_{tp}\sum_{\ell q}\left\langle\lambda\ell,1(-q)|\mathrm{tp}\right\rangle(-1)^q\langle\psi_i|\boldsymbol{U}^{(\lambda)}_{\ell}\left|\psi_f\right\rangle\right|^2+\left|\langle\psi_i|\boldsymbol{m}\left|\psi_f\right\rangle\right|^2 \quad (13)$$

where $q=0,\ \pm1$, $\ell=p+q$, and p is restricted by the D_2 site symmetry to even integers with $|p|\le t$. The first term, giving the electric-dipole contribution is parameterized by the A^{λ}_{tp} parameters and use calculated $U^{(\lambda)}_{\ell}$ matrix elements. The second term gives the magnetic-dipole contribution and is calculated directly. For ground-state transitions of Er^{3+}, only the $^4I_{15/2}\to{}^4I_{13/2}$, $^2K_{15/2}$, and $^2K_{13/2}$ transitions have a magnetic dipole contribution greater than 2% of the observed intensity.

For D_2 site symmetry, there are 18 independent A^{λ}_{tp} parameters, nine of which are allowed under the "superposition model" approximation, and an additional nine parameters which can arise only through non-cylindrically symmetric ligand/ion interactions. Previous work has shown that the additional "non-superposition model" parameters are necessary to adequately rationalize transition line strengths in the YAG system.[40]

As was the case for the crystal-field and correlation-crystal-field energy level parameters, calculated intensity parameter values for transitions between Stark levels are dependent upon the crystal-field parameter axes orientation selected. As well, it is now known that once the crystal-field parameter axes are selected, there are additional ambiguities in the intensity parameters that yield multiple sets of different parameter values which give identical calculated intensities.

In order to rationalize these multiple sets of different parameters, we use an alternative "vector crystal field" parametrization, $B^{\lambda}_{\ell q}$,[41] which yields the following expansion for transition line strengths,

$$S_{i\to f}=e^2\left|\sum_{\lambda\ell q}B^{\lambda}_{\ell q}\langle\psi_i|\boldsymbol{U}^{(\lambda)}_{\ell}\left|\psi_f\right\rangle\right|^2+\left|\langle\psi_i|\boldsymbol{m}\left|\psi_f\right\rangle\right|^2 \quad (14)$$

Comparing Eq. (14) with Eq. (13), we see there is a direct linear transformation between the $B^{\lambda}_{\ell q}$ and A^{λ}_{tp} parametrizations, given by,

$$B^{\lambda}_{(p+q)q}=\sum_t A^{\lambda}_{tp}(-1)^q\langle\lambda(p+q),1-q|tp\rangle \quad (15)$$

where $q=0,\ \pm1$ represent the spherical polarization bases.

For D_2 symmetry, there are three independent polarization directions of the radiation field: *x, y,* and *z*. The "vector crystal field" $B^{\lambda}_{\ell q}$ parameters may be separated into subsets specific for each independent polarization by the spherical to Cartesian transformation,

$$B^{\lambda}_{\ell x}=\left(-B^{\lambda}_{\ell 1}+B^{\lambda}_{\ell -1}\right)/\sqrt{2},\ B^{\lambda}_{\ell y}=i\left(B^{\lambda}_{\ell 1}+B^{\lambda}_{\ell -1}\right)/\sqrt{2},\quad B^{\lambda}_{\ell z}=B^{\lambda}_{\ell 0} \quad (16)$$

This transformation yields six *x*-polarization $B^{\lambda}_{\ell x}$ parameters, six *y*-polarization $B^{\lambda}_{\ell y}$ parameters, and six *z*-polarization $B^{\lambda}_{\ell z}$ parameters. Transformation matrices between the A^{λ}_{tp} and $B^{\lambda}_{\ell i}$ ($i=x, y, z$) parameterizations for D_2 symmetry have been presented elsewhere.[42]

In this alternative vector-crystal-field parameterization, the multiplicity of parameter sets is resolved as independent overall signs on each separated-polarization subset of parameters. Thus, for D_2 symmetry, with three independent polarization directions, there are $(2)^3=8$ different parameter sets yielding identical line strengths.

Table 5 presents the $B^{\lambda}_{\ell i}$ parameters fitted to 88 ground-state transitions by minimizing the standard deviation,

$$\sigma=\sqrt{\sum_i\frac{\left[(E_i-C_i)/E_i\right]^2}{N-P}} \quad (17)$$

where E_i and C_i are the experimental and calculated values, respectively, $N=88$ data points and $P=18$ parameters. The fitting standard deviation is $\sigma=0.28$ (r.m.s. error $=0.25$), representing a 25% overall deviation between experimental and calculated values. Using a method of random starting parameter values,[43,44] we found that this is an extremely robust solution, with the eight-fold minimum being the only minimum that is found from all reasonable ranges of starting parameters. This is in marked contrast to previous calculations of

TABLE 5 **Intensity Parameters in Vector Crystal-Field Notation Corresponding to the Six Different Parameterizations Given in Table 1. Sets "a" ("b") correspond to the top (bottom) signs for the $q=2$, 6 parameters given in Table 1. The $B^{\lambda}_{\ell x}$ and $B^{\lambda}_{\ell z}$ parameters have units $i\times10^{-12}$ cm; $B^{\lambda}_{\ell y}$ parameters have units 1×10^{-12} cm. The Ω_{λ} parameters have units 10^{-20} cm^2. Each parameter set presented here represents one of eight parameter solutions–the other seven parameterizations are derived from these by combinations of changing the sign on all $B^{\lambda}_{\ell x}$ parameters, all $B^{\lambda}_{\ell y}$ parameters, and/or all $B^{\lambda}_{\ell z}$ parameters.**

Parameter	Set 1a	Set 1b	Set 2a	Set 2b	Set 3a	Set 3b
B^2_{1x}	36 (14)	−81 (13)	81 (13)	−174 (12)	174 (12)	−36 (14)
B^2_{1y}	81 (13)	36 (14)	174 (12)	81 (13)	36 (14)	174 (12)
B^2_{2z}	174 (12)	−174 (12)	36 (14)	−36 (14)	81 (13)	−81 (13)
B^4_{1x}	165 (14)	25 (13)	16 (14)	28 (15)	104 (11)	−6 (12)
B^4_{1y}	−25 (13)	165 (14)	−28 (15)	16 (14)	6 (12)	104 (11)
B^4_{2z}	−107 (13)	107 (13)	−241 (10)	241 (10)	12 (16)	−12 (16)
B^4_{3x}	−196 (9)	−3 (16)	19 (15)	125 (11)	−75 (15)	256 (12)
B^4_{3y}	−3 (16)	196 (9)	125 (11)	−19 (15)	256 (12)	75 (15)
B^4_{4z}	−70 (13)	−70 (13)	−85 (13)	−85 (13)	−22 (13)	−22 (13)
B^6_{1x}	−59 (11)	78 (7)	−5 (6)	−33 (7)	101 (8)	200 (10)
B^6_{1y}	−78 (7)	−59 (11)	33 (7)	−5 (6)	−200 (10)	101 (8)
B^6_{2z}	−101 (9)	101 (9)	−52 (8)	52 (8)	55 (6)	−55 (6)
B^6_{3x}	−145 (9)	1 (7)	−116 (7)	−157 (8)	49 (8)	−78 (10)
B^6_{3y}	1 (7)	145 (9)	−157 (8)	116 (7)	−78 (10)	−49 (8)
B^6_{4z}	79 (8)	79 (8)	162 (11)	162 (11)	84 (7)	84 (7)
B^6_{5x}	−152 (9)	−87 (6)	−12 (7)	25 (9)	−117 (9)	−39 (9)
B^6_{5y}	87 (6)	−152 (9)	−25 (9)	−12 (7)	39 (9)	−117 (9)
B^6_{6z}	99 (7)	−99 (7)	−136 (10)	136 (10)	−60 (6)	60 (6)
Ω_2	1.53	1.53	1.53	1.53	1.53	1.53
Ω_4	1.83	1.83	1.83	1.83	1.83	1.83
Ω_6	1.34	1.34	1.34	1.34	1.34	1.34
Ω_{2x}	0.05	0.26	0.26	1.22	1.22	0.05
Ω_{2y}	0.26	0.05	1.22	0.26	0.05	1.22
Ω_{2z}	1.22	1.22	0.05	0.05	0.26	0.26
Ω_{4x}	1.45	0.01	0.01	0.37	0.37	1.45
Ω_{4y}	0.01	1.45	0.37	0.01	1.45	0.37
Ω_{4z}	0.37	0.37	1.45	1.45	0.01	0.01
Ω_{6x}	0.73	0.21	0.21	0.40	0.40	0.73
Ω_{6y}	0.21	0.73	0.40	0.21	0.73	0.40
Ω_{6z}	0.40	0.40	0.73	0.73	0.21	0.21

Nd:YAG[45] and oxydiacetate systems,[44,46] where dozens of local minima have been found. This provides us with some degree of confidence that the measured intensities are self-consistent and that the calculated parameter values are reliable. Experimental intensities are well reproduced by the calculation for all measured absorption lines except for the third and fourth levels of the $^4F_{9/2}$ multiplet (levels 29 and 30 in Table 4), which are underestimated by factors of 25 and 7, respectively. We do not have an explanation for this anomaly, but when these two levels are excluded, the r.m.s. error for the remaining levels is under 0.21.

The six numerical columns of Table 5 present parameter values for each of the six crystal-field axes orientations given in Table 1. Sets "*a*" correspond to the top signs for the p = 2, 6 parameters given in Table 1, while sets "*b*" correspond to the bottom signs. Each set of parameter values presented in Table 5 represents an eight-fold solution. The other seven solutions can be derived from the one presented in Table 5 by independently changing the sign on all $B^{\lambda}_{\ell x}$ parameters, changing the sign on all $B^{\lambda}_{\ell y}$ parameters, and/or changing the sign on all $B^{\lambda}_{\ell z}$ parameters. When standard A^{λ}_{tp} parameters are used, these eight solutions result in different values for each of the A^{λ}_{tp} parameters.[42,43] Values presented in Table 5 differ slightly from our preliminary paper[42] due to a correction in identification of Morrison and Leavitt sets 1 and 3, and a more accurate determination of the Er^{3+} ion concentration in the crystal.

It is possible to define electric-dipole intensity interaction strength parameters analogous to those defined for the crystal-field interaction strength in Eq. (11), though omitting the square root. This gives us, in terms of the standard A^{λ}_{tp} parameters, overall intensity parameters,

$$\begin{aligned}\Omega_{\lambda} &= \frac{1}{2\lambda+1}\sum_{tp}\left|A^{\lambda}_{tp}\right|^2 \\ &= \frac{1}{2\lambda+1}\sum_{t}\left[\left(A^{\lambda}_{t0}\right)^2 + 2\sum_{p>0}\left|A^{\lambda}_{tp}\right|^2\right] \end{aligned} \quad (18)$$

These Ω_{λ} parameters are simply the Judd-Ofelt intensity parameters for multiplet-to-multiplet transitions. That is, under the specific conditions that the individual Stark levels within each of the initial and final multiplets can be considered to be essentially degenerate, each Stark level of the initial multiplet can be considered to be essentially equally populated, and the initial and final multiplet states have well defined J character, summing the electric-dipole contribution of Eq. (13) over all Stark levels of the initial and final multiplets gives,

$$\begin{aligned}S^{\mathrm{ED}}_{\psi J\rightarrow\psi' J'} &= e^2\sum_{\lambda tp}\frac{1}{2\lambda+1}\left|A^{\lambda}_{tp}\right|^2\left\langle \psi J\left\| U^{(\lambda)}\right\|\psi' J'\right\rangle^2 \\ &= e^2\sum_{\lambda}\Omega_{\lambda}\left\langle \psi J\left\| U^{(\lambda)}\right\|\psi' J'\right\rangle^2 \end{aligned} \quad (19)$$

where the second line is the famous Judd-Ofelt equation. As the specific conditions requiring the absence of crystal-field mixings of different J-multiplets and the absence of crystal-field splittings within the multiplets are not well-met in real systems, one would not expect the Ω_{λ} parameters calculated from the A^{λ}_{tp} to be equal to published Ω_{λ} parameters from multiplet-to-multiplet fittings. However, treated as interaction-strength parameters, they provide rotationally invariant values that may be used for comparison purposes.

Alternatively, we can use the vector crystal field $B^{\lambda}_{\ell q}$ parameters to define the Ω_{λ} parameters. Rewriting Eq. (18) in terms of the $B^{\lambda}_{\ell q}$ gives,

$$\begin{aligned}\Omega_{\lambda} &= \frac{1}{2\lambda+1}\sum_{\ell q}\left|B^{\lambda}_{\ell q}\right|^2 \\ &= \frac{2}{2\lambda+1}\sum_{\ell>0}\left(\left|B^{\lambda}_{\ell x}\right|^2+\left|B^{\lambda}_{\ell y}\right|^2+\left|B^{\lambda}_{\ell z}\right|^2\right) \end{aligned} \quad (20)$$

where the 2 on the right hand side comes from $\ell =$ negative contributions to the summation.

The bottom section of Table 5 presents Ω_{λ} parameters calculated from Eq. (20). From this table, it can be seen that the Ω_{λ} parameters are invariant with respect to both the crystal-field parameterization used and the multiple parameter solutions that arise within a particular crystal-field parameterization. These values are $\Omega_2 = 1.53\times10^{-20}\,\mathrm{cm}^2$, $\Omega_4 = 1.83\times10^{-20}\,\mathrm{cm}^2$, and $\Omega_6 = 1.34\times10^{-20}\,\mathrm{cm}^2$.

For comparison, literature values of the Judd-Ofelt parameters are, $\Omega_2 = 0.740\times10^{-20}\,\mathrm{cm}^2$, $\Omega_4 = 0.330\times10^{-20}\,\mathrm{cm}^2$, and $\Omega_6 = 1.020\times10^{-20}\,\mathrm{cm}^2$, from Kaminskii,[1] and $\Omega_2 = 0.724\times10^{-20}\,\mathrm{cm}^2$, $\Omega_4 = 0.327\times10^{-20}\,\mathrm{cm}^2$, and $\Omega_6 = 0.790\times10^{-20}\,\mathrm{cm}^2$, from Sardar et al.[8] These values are the same order of magnitude, but somewhat smaller than our calculated values, a phenomenon that has been observed previously for Nd:YAG.[41]

As can be seen from the right hand side of Eq. (20), the contributions from each of the three polarizations are separable, allowing one to define polarization-dependent Judd-Ofelt parameters,

$$\begin{aligned}&\Omega_{\lambda x} = \frac{2}{2\lambda+1}\sum_{\ell>0}\left|B^{\lambda}_{\ell x}\right|^2, \quad \Omega_{\lambda y} = \frac{2}{2\lambda+1}\sum_{\ell>0}\left|B^{\lambda}_{\ell y}\right|^2, \\ &\Omega_{\lambda z} = \frac{2}{2\lambda+1}\sum_{\ell>0}\left|B^{\lambda}_{\ell z}\right|^2 \end{aligned} \quad (21)$$

where,

$$\Omega_{\lambda} = \Omega_{\lambda x} + \Omega_{\lambda y} + \Omega_{\lambda z} \quad (22)$$

The bottom section of Table 5 presents the complete Judd-Ofelt parameters Ω_{λ} along with the separated-polarization $\Omega_{\lambda x}$, $\Omega_{\lambda y}$, and $\Omega_{\lambda z}$ terms. As we have already seen, the Ω_{λ} parameters are invariant with respect to coordinate rotations. But more than this, as can be seen from Table 5, each of the six sets of $B^{\lambda}_{\ell i}$ ($i = x, y, z$) parameters yields identical $\Omega_{\lambda i}$ parameter values, but with the x, y, and z subscripts permuted in all six possible ways. This means the $\Omega_{\lambda i}$ may be uniquely identified with the crystallographic a, b, and c axis directions, independent of the choice of quantization axes.

This provides justification for the idea of formally separating polarization-dependent parts of the Judd-Ofelt parameters. Presentation of separated polarization-dependent parts of the Judd-Ofelt parameters can provide greater information than

the current practice of presenting only one set of (isotropic) Judd-Ofelt parameters. See, for example, Sardar and Bella,[47] where polarization-dependent multiplet-to-multiplet measurements were taken, but only isotropic Judd-Ofelt parameters were reported.

CONCLUSION

In this study, we provide a comprehensive review of the energy (Stark) levels of $Er^{3+}(4f^{11})$ in YAG and the intensity of the absorption transitions from the ground-state Stark level to individual excited Stark levels having an energy up to $50{,}000\,cm^{-1}$. Within this energy range, 125 experimental Stark levels and 88 experimental transition line strengths are analyzed in detail with a standard deviation of $12.7\,cm^{-1}$ (r.m.s. deviation of $11.2\,cm^{-1}$) for the energy levels, and a weighted $(E_i - C_i)/E_i$ standard deviation of 0.28 (r.m.s. deviation of 0.25) for the transition line strengths.

We present six sets of crystal-field parameters arising from the six alternative choices for parametrization axes in D_2 symmetry, and calculate intensity parameters based upon each of these six parametrizations. The eightfold sets of intensity parameters arising from each parametrization have been resolved as three arbitrary sign choices for each polarization subset of the vector crystal field parameters. The vector crystal field parametrization also leads to a new definition for polarization-resolved Judd-Ofelt parameters, which have the potential to have wide-ranging applicability for future polarized Judd-Ofelt-type intensity calculations.

ACKNOWLEDGMENTS

This research was supported in part by the American Chemical Society Grant No. PRF 43862-B6 and the National Science Foundation Grant No. DMR-0602649.

REFERENCES

1. Kaminskii, A. A. *Laser Crystals*; Springer: New York, 1981.
2. Koechner, W. *Solid State Laser Engineering*; Springer: New York, 1996.
3. Ranin, R.M. *Erbium-Doped Fiber Lasers*; Springer: New York, 1997.
4. Young, Y. E.; Setzler, S. D.; Snell, K. J.; Budni, P. A.; Pollak, T. M.; Chicklis, E. P. Efficient 1645-nm Er:YAG laser. *Opt. Lett.* **2004**, *29*, 1075–1077.
5. Kaminskii, A. A. *Crystalline Lasers: Physical Processes and Operating Schemes*; CRC: New York, 1996.
6. Gruber, J. B.; Sardar, D. K.; Zandi, B. J.; Hutchinson, A.; Trussell, C. W. Modeling the absorption spectra of Er^{3+} and Yb^{3+} in a phosphate glass. *J. Appl. Phys.* **2003**, *94*, 4835–4840, and references therein.
7. Lippert, E.; Rustad, G.; Stenersen, K. *OSA Trends in Optics and Photonics Series, Advanced Solid-State Photonics*; Optical Society of America: Washington, D.C., 2003, *83*, 266.
8. Sardar, D. K.; Russell III, C. C.; Gruber, J. B.; Allik, T. H. Absorption intensities and emission cross sections of principal intermanifold and inter-Stark transitions of Er^{3+}:4f ^{11} in polycrystalline ceramic garnet $Y_3Al_5O_{12}$. *J. Appl. Phys.* **2005**, *97*, 123501.
9. Garbuzov, D.; Kudryashov, I.; Dubinskii, M. Resonantly diode laser pumped 1.6-μm-erbium-doped yttrium aluminum garnet solid-state laser. *Appl. Phys. Lett.* **2005**, *86*, 131115.
10. Spariosu, K.; Leyva, V.; Reeder, R. A.; Klotz, M. J. Efficient Er : YAG laser operating at 1645 and 1617 nm. *IEEE J. Quantum Electron.* **2006**, *42*, 182–186. and references therein.
11. Gruber, J. B.; Nijjar, A. S.; Sardar, D. K.; Yow, R. M.; Russell III, C. C.; Allik, T. H.; Zandi, B. Spectral analysis and energy-level structure of $Er^{3+}(4f^{11})$ in polycrystalline ceramic garnet $Y_3Al_5O_{12}$. *J. Appl. Phys.* **2005**, *97*, 063519.
12. Koningstein, J. A.; Geusic, G. E. Energy levels and crystal-field calculations of neodymium in yttrium aluminum garnet. *Phys. Rev.* **1964**, *136*, A711–A716.
13. Zverev, G. M.; Kolodnyĭ, G. Ya.; Onishchenko, A. M. Resonant and nonresonant processes of excitation energy transfer from Tu^{3+} or Ho^{3+} ions to the Er^{3+} ions in $(Y,Er)_3Al_5O_{12}$ crystals. *Sov. Phys. JETP*, **1970**, *30*, 435–440. (*Zh. Eksp. Teor. Fiz.*, **1969**, *57*, 794–805.)
14. Kaminskii, A. A.; Butaeva, T. I.; Fedorov, V. A.; Bagdasarov, Kh. S.; Petrosyan, A. G. Absorption, luminescence, and stimulated emission investigations in $Lu_3Al_5O_{12}$-Er^{3+} crystals. *Phys. Stat. Sol. (a)*. **1977**, *39*, 541–548.
15. Morrison, C. A.; Leavitt, R. P. In *Handbook on the Physics and Chemistry of the Rare Earths*; Gschneidner, K.A., Jr., Eyring, L., Eds.; North-Holland: Amsterdam, 1982, 632–642.
16. Gruber, J. B.; Quagliano, J. R.; Reid, M. F.; Richardson, F. S.; Hills, M. E.; Seltzer, M. D.; Stevens, S. B.; Morrison, C. A.; Allik, T. H. Energy levels and correlation crystal-field effects in Er^{3+}-doped garnets. *Phys. Rev. B*. **1993**, *48*, 15561–15573.
17. Kokta, M. Solubility enhancement of Nd^{3+} in scandium-substituted rare earth-aluminum garnets. *J. Solid State Chem.* **1973**, *8*, 39–42.
18. Brandle, C. D.; Barns, R. L. Crystal stoichiometry of Czochralski grown rare-earth gallium garnets. *J. Cryst. Growth*, **1974**, *26*, 169–170.
19. Carnall, W. T.; Goodman, G. L.; Rajnak, K.; Rana, R. S. A systematic analysis of the spectra of the lanthanides doped into single-crystal LaF_3. *J. Chem. Phys.* **1989**, *90*, 3443–3457.
20. Morrison, C. A. *Angular Momentum Theory Applied to Interactions in Solids*; Springer: New York, 1988.
21. Chen, X.; Liu, G.; Margerie, J.; Reid, M. F. A few mistakes in widely used data files for f(n) configurations calculations. *J. Lumin.* **2008**, *128*, 421–427.
22. Judd, B. R. Ligand field theory for actinides. *J. Chem. Phys.* **1977**, *66*, 3163–3170.
23. Reid, M. F. Correlation crystal field analyses with orthogonal operators. *J. Chem. Phys.* **1987**, *87*, 2875–2884.
24. Judd, B. R. Ligand polarizations and lanthanide ion spectra. In *Lecture Notes in Physics*; Kramer, P., Rieckers, A., Eds.; Springer: Berlin, 1978, 417–419.
25. Burdick, G. W.; Richardson, F. S. Application of the correlation-crystal-field delta-function model in analyses of $Pr^{3+}(4f^2)$ energy-level structures in crystalline hosts. *Chem. Phys.* **1998**, *228*, 81–101.
26. Quagliano, J. R.; Burdick, G. W.; Glover-Fischer, D. P.; Richardson, F. S. Electronic absorption spectra, optical line strengths, and crystal-field energy-level structure of Nd^{3+} in hexagonal $[Nd(H_2O)_9](CF_3SO_3)_3$. *Chem. Phys.* **1995**, *201*, 321–342.
27. McAven, L. F.; Reid, M. F.; Butler, P. H. Transformation properties of the delta-function model of correlation crystal fields. *J. Phys. B: At. Mol. Opt. Phys.* **1996**, *29*, 1421–1431; erratum, *ibidem,* 4319.

28. Rudowicz, C.; Qin, J. Can the low symmetry crystal (ligand) field parameters be considered compatible and reliable? *J. Lumin.* **2004**, *110*, 39–64.
29. Burdick, G. W.; Reid, M. F. Crystal field parametrizations for low symmetry systems. *Mol. Phys.* **2004**, *102*, 1141–1147.
30. Morrison, C. A.; Wortman, D. E.; Karayianis, N. Crystal-field parameters for triply-ionized lanthanides in yttrium aluminium garnet. *J. Phys. C: Solid State Phys.* **1976**, *9*, L191–L194.
31. Rudowicz, C.; Bramley, R. On standardization of the spin Hamiltonian and the ligan field Hamiltonian for orthorhombic symmetry. *J. Chem. Phys.* **1985**, *83*, 5192–5197.
32. Gruber, J. B.; Nash, K. L.; Yow, R. M.; Sardar, D. K.; Valiev, U. V.; Uzokov, A. A.; Burdick, G. W. Spectroscopic and magnetic susceptibility analyses of the ^7F_J and $^5D_4$ energy levels of Tb^{3+} ($4f^8$) in $TbAlO_3$. *J. Lumin.* **2008**, *128*, 1271–1284.
33. Gruber, J. B.; Chandra, S.; Sardar, D. K.; Valiev, U. V.; Juraeva, N. I.; Burdick, G. W. Modeling optical spectra and Van Vleck paramagnetism in Er^{3+}:$YAlO_3$. *J. Appl. Phys.* **2009**, *105*, 023112, 13 pages.
34. Rudowicz, C.; Chua, M.; Reid, M. F. On the standardization of crystal-field parameters and the multiple correlated fitting technique: Applications to rare-earth compounds. *Physica B*. **2000**, *291*, 327–338.
35. Leavitt, R. P. On the role of certain rotational invariants in crystal-field theory. *J. Chem. Phys.* **1982**, *77*, 1661–1663.
36. Chang, N. C.; Gruber, J. B.; Leavitt, R. P.; Morrison, C. A. Optical-spectra, energy-levels, and crystal-field analysis of the tripositive rare-earth ions in Y_2O_3. 1. Kramers ions in C_2 sites. *J. Chem. Phys.* **1982**, *76*, 3877–3889.
37. Rudowicz, C.; Qin, J. Noether theorem for the crystal (ligand) field Hamiltonians and the zero-field splitting Hamiltonians invariant under continuous symmetry. *Phys. Rev. B*. **2003**, *67*, 174420, 14 pages.
38. Reid, M. F.; Richardson, F. S. Electric-dipole intensity parameters for lanthanide $4f \rightarrow 4f$ tranistions. *J. Chem. Phys.* **1983**, *79*, 5735–5742.
39. Reid, M. F.; Richardson, F. S. Lanthanide $4f \rightarrow 4f$ electric-dipole intensity theory. *J. Phys. Chem.* **1984**, *88*, 3579–3586.
40. Burdick, G. W.; Jayasankar, C. K.; Richardson, F. S.; Reid, M. F. Energy-level and line-strength analysis of optical transitions between Stark levels in Nd^{3+}:$Y_3Al_5O_{12}$. *Phys. Rev. B.* **1994**, *50*, 16309–16325.
41. Burdick, G. W.; Crooks, S. M.; Reid, M. F. Ambiguities in the parametrization of $4f^n$-$4f^n$ electric-dipole transition intensities. *Phys. Rev. B.* **1999**, *59*, R7789–R7792.
42. Burdick, G. W.; Gruber, J. B.; Nash, K. L.; Chandra, S.; Sardar, D. K. Electric-dipole $4f^{11}$-$4f^{11}$ transition Intensities measured and calculated between Stark components in Er^{3+}:$Y_3Al_5O_{12}$. *J. Alloys. Comp.* **2009**, *488*, 632–637.
43. Burdick, G. W.; Summerscales, R. L.; Crooks, S. M.; Reid, M. F.; Richardson, F. S. Electric-dipole $4f^n$-$4f^n$ transition intensity parametrizations for lanthanides: Multiple indistinguishable parameter sets and multiple local minima. *J. Alloys Comp.* **2000**, *303*, 376–382.
44. Burdick, G. W.; Yim, Y.; LaBianca, E. S. Judd-Ofelt parametrizations for lanthanides: Sensitivity analysis of multiple local minima. *Mol. Phys.* **2003**, *101*, 909–916.
45. Crooks, S. M.; Reid, M. F.; Burdick, G. W. Fitting of parameters to represent the circular dichroism and transition intensities of $4f^n$-$4f^n$ transitions of lanthanide ions. *J. Alloys Comp.* **2000**, *303*, 383–386.
46. Burdick, G. W.; Robertson, R. D.; Summerscales, R. L. Electric-dipole $4f^n$-$4f^n$ transition intensity parametrizations for lanthanides: An examination of multiple local minima. *J. Alloys Comp.* **2001**, *323*, 778–782.
47. Sardar, D. K.; Bella, P. D. Optical Characterization of Nd^{3+}:$Sr_5(VO_4)_3F$. *J. Appl. Phys.* **1994**, *76*, 5900–5904.